



1 **Beyond and beneath displacement time series: towards InSAR-based early warnings and**
2 **deformation analysis of the Achoma landslide, Peru**

3

4 Benedetta Dini^{1,2}, Pascal Lacroix², Marie-Pierre Doin²

5 ¹School of Geography, Earth and Environmental Sciences, University of Birmingham, Birmingham, UK

6 ²ISTerre, Université Grenoble-Alpes, Grenoble, France

7

8 Corresponding author:

9 Benedetta Dini, School of Geography, Earth and Environmental Sciences, University of Birmingham,
10 Birmingham, UK

11 Formerly at: ISTerre, Université Grenoble-Alpes, Grenoble, France

12 orcid number: 0000-0002-1578-7294

13 Email address: b.dini@bham.ac.uk

14

15 **Abstract**

16 Detecting precursors to slope destabilisation with sufficient lead time and accuracy remains
17 a challenging and unresolved issue in landslide hazard assessment and prediction. This is key,
18 as catastrophic landslides often go unnoticed until immediately before failure, limiting
19 opportunities for intervention. While in situ methods offer high accuracy at point locations,
20 they are costly and require prior knowledge of instability. Satellite-based synthetic aperture
21 radar differential interferometry (InSAR) has shown promise in identifying unknown
22 landslides over large areas and has been proposed as a potentially useful tool for failure
23 prediction. Typically valued for retrieving displacement time series, InSAR time series
24 reliability depends heavily on successful interferogram unwrapping, which often leads to
25 severe underestimations over landslides. Here, we analyse the deformation process of the
26 Achoma landslide in Peru and demonstrate that the InSAR signal contains precursors based
27 on alternative markers, even without displacement time series. Interferometric coherence
28 shows the formation of gravitational structures up to five years before failure, as well as a
29 critical shift in landslide behaviour three months prior to failure. Additionally, a marker based
30 on the wrapped phase reveals and quantifies alternating periods of quiescence and motion,
31 the latter becoming more frequent in the two years before failure. Our findings highlight the
32 potential to use alternative InSAR signal markers to observe the deformation process and



33 progressive failure leading up to the event, and to detect landslide precursors across
34 extensive areas, providing valuable lead time for intervention and disaster prevention.

35

36 **Keywords:**

37 InSAR - Landslide precursors – Incipient slope destabilisation - Early warning indicators
38 Progressive failure – Landslide dynamics – Interferometric coherence - Interferometric
39 wrapped phase

40

41 **1. Introduction**

42 Landslides pose a global threat, causing approximately 14,000 fatalities annually (Petley 2012)
43 including more than 4,000 resulting from non-seismic triggers (Froude and Petley 2018).
44 Beyond the human toll, landslides lead to substantial social and economic consequences in
45 both developing and developed countries. Despite advances in hazard assessment, predicting
46 when and where potentially unstable hillslopes will fail catastrophically remains a major
47 challenge. This highlights the critical importance of early identification of destabilizing slopes
48 and the detection of accelerating phases, which are key to improving prediction and
49 preparedness (e.g., Carlà et al. 2017a; Roy et al. 2022; Valletta et al. 2022; Strząbała et al.
50 2024).

51 While there are documented instances of successful predictions and early warnings using in-
52 situ methods (e.g., Badoux et al. 2009; Loew et al. 2017; Fan et al. 2019), two main challenges
53 persist: cost and feasibility of monitoring all known unstable slopes, and the limited pre-
54 existing knowledge of instability, which often leads to landslides remaining unnoticed until
55 severe acceleration or catastrophic failure occurs (Palmer 2017; Guzzetti 2021), causing
56 significant delays in the installation of monitoring systems (e.g., Fiolleau et al. 2020).

57 The advent and use of satellite-based technologies, particularly satellite-based synthetic
58 aperture radar differential interferometry (InSAR), have significantly improved landslide
59 identification capabilities (e.g. Strząbała et al. 2024). Observations can be made more cost-
60 effectively due to the increasing availability, frequency, and reliability of acquisitions, whilst
61 the large coverage (Costantini et al. 2021; Lacroix et al. 2021; Wasowski and Bovenga 2022)
62 may allow for the identification of previously unknown unstable slopes at large scales (Dini et
63 al. 2019, 2020). This enhances the possibility of implementing timely and targeted monitoring



64 before disasters occur. Identifying destabilising slopes from satellite data is crucial also for
65 landslides in remote locations, which are challenging to spot and monitor in-situ, yet can
66 generate far-reaching hazard cascades (Cook et al. 2021). With increasing temporal sampling
67 of new generation satellites and the potential for sub-centimetre displacement accuracy in
68 favourable conditions (Ferretti et al. 2011; Liu et al. 2013; Wasowski and Bovenga 2014), the
69 use of InSAR has become widespread for generating landslide displacements time series
70 based on small baseline subset (Berardino et al. 2002) (SBAS) or permanent scatterers
71 (Ferretti et al. 2001, 2005) (PS) algorithms, and variations of these. In a few cases,
72 retrospective retrieval of time series revealed acceleration patterns leading to failure,
73 highlighting potential for accurate prediction of failure timing (Intrieri et al. 2018; Carlà et al.
74 2019).

75 However, despite InSAR's remarkable potential for geohazard observation, the universal
76 reliability of InSAR displacement time series is not guaranteed, due to significant challenges
77 related to the nature of the phenomena and data processing limitations. We highlight here
78 only the limitations relevant to this work. For a more exhaustive account we refer to Lacroix
79 et al. (2021) and references therein.

80 Small to medium-size landslides (a few tens to a few hundred m along-scarp length) in many
81 cases only cover a relatively small number of SAR pixels on the ground (e.g., for the pixel size
82 of Sentinel-1, 2.3 m by 14.1 m), making signal detection challenging. Larger landslides (several
83 hundred m along-scarp length) may exhibit displacements only on isolated sectors at different
84 times. Additionally, landslides often present strong spatial gradients and sharp displacement
85 edges that make phase unwrapping problematic due to phase aliasing (Manconi 2021;
86 Strząbała et al. 2024). Finally, landslides often display non-linear behaviour in time, with
87 phases of accelerations interspersed with periods of quiescence. This is unfavourable for
88 InSAR time series based on SBAS or PS approaches, particularly when temporal sampling is
89 affected by missing acquisitions or unusable images (e.g., snow cover, seasonal landcover
90 changes). When a slope transitions from no displacement to fast reactivation, with
91 displacements exceeding a threshold (commonly $\frac{1}{4}$ of the wavelength) between two
92 acquisitions and/or between adjacent pixels when gradients are strong, phase aliasing and
93 decorrelation occur. The lack of phase continuity makes it difficult to accurately reconstruct
94 the continuous phase signal from the wrapped phase measurements. As conventional
95 processing methods for generating displacement time series rely on phase unwrapping, they



96 are particularly susceptible to phase aliasing (Manconi 2021). Moreover, as interferometric
97 coherence decreases, unwrapping over critical areas might not be performed when
98 processing large areas due to the cutoff imposed using coherence thresholds. This leads to
99 the loss of any true deformation signal potentially contained in low- (or lower-) coherence
100 interferograms. In essence, the success on landslide of common InSAR approaches heavily
101 relies on the existence of many conditions favourable to processing. Without individual
102 interferogram inspection, a time consuming task, an InSAR displacement time series might
103 seem accurate and plausible, yet it could significantly underestimate the true displacements
104 and obscure crucial acceleration phases and/or their magnitude (Dini et al. 2020; Jacquemart
105 and Tiampo 2021). Consequently, there is a high potential for misinterpreting the ongoing
106 processes driving instability and assessing the hazard level.

107 In response to the challenges associated with InSAR, some authors focused on the analysis of
108 high-frequency optical images (e.g., Sentinel-2, PlanetLab) to derive time series of
109 displacements (Lacroix et al. 2018, 2023), or changes in vegetation cover caused by landslides
110 with NDVI from Sentinel-2 acquisitions (Yang et al. 2019). However, optical data are
111 constrained by cloud coverage and have limited sensitivity to smaller displacements that
112 might occur over longer time frames leading up to failure. Others have successfully retrieved
113 acceleration phases through optical image correlation of SAR images (Li et al. 2020), but this
114 method is also limited to the observation of relatively large displacements (greater than 1/10
115 of the pixel size), thus more suitable to cover the final weeks to months of an accelerating
116 phase. Consequently, alternative and/or complementary InSAR-based techniques must be
117 developed to improve our ability to observe landslide precursors beyond what is possible
118 using only methods reliant on phase unwrapping. Jacquemart et al. (2021) focused on InSAR
119 coherence, showing a temporal decrease of coherence roughly 5 months prior to the
120 Mudcreek landslide failure. To our knowledge this is the only study on this topic, highlighting
121 the need for more case-studies and in-depth understanding of landslide behaviours
122 associated with this type of signal.

123 Our work introduces a novel methodology for extracting landslide precursors that bypasses
124 traditional time series generation. Instead, we integrate information on incipient and ongoing
125 instability using interferometric coherence and wrapped phase. This approach is particularly
126 valuable when full displacement time series are unavailable or unreliable. By addressing the
127 limitations of conventional methods, we offer an alternative perspective on landslide



128 precursor identification from space. This paper explores two critical questions: Can
129 interferometric coherence serve as an effective precursor for identifying critical landslide
130 phases and incipient instability in both time and space? And can indicators based on the
131 wrapped phase provide insights into criticality of landslide behaviour, in the absence of a
132 reliable displacement time series?

133 To illustrate our methodology, we present a case study on the Achoma landslide in the Colca
134 Valley, Peru. This landslide exemplifies an instability that remained unnoticed on the ground
135 until shortly before catastrophic failure, while retrospective analysis using optical satellite
136 images detected signals three months before the event (Lacroix et al. 2023). Remarkably, our
137 results show that signs of destabilisation were detectable five years prior to failure. The
138 subsequent sections of this paper detail the methods we employed, including topographic
139 error correction, coherence loss analysis, and the extraction of wrapped phase temporal
140 behaviour. Finally, we present our results and discuss their significance, highlighting the
141 potential integration of our approach with traditional methods.

142

143 **2. Study area**

144 The deeply incised Colca Valley is located in southern Peru. On its terraces, it hosts several
145 settlements, largely supported by extensive agriculture. The valley is located between
146 volcanic massifs to the north and south (Zerathe et al. 2016), and is characterised by
147 sequences of ignimbrites and pyroclastic deposits. The valley's geomorphology has been
148 shaped by debris avalanches from valley flank collapses followed by landslide dam breakouts
149 (Thouret et al. 2007), with one such event forming a paleolake and depositing thick lacustrine
150 deposits (Lacroix et al. 2015; Zerathe et al. 2016).

151 Seismicity in the region has distinct sources (Zerathe et al. 2016; Lacroix et al. 2023 and
152 references therein), from relatively low magnitude ($M_w < 3$) seismic events originating in the
153 volcanic area approximately 15-20 km to the southwest, to larger magnitude earthquakes
154 associated with regional tectonic faults ($M_w < 7$) or $M_w 8$ events with origin in the subduction
155 zone roughly 100 km to the west.

156 The area experiences a seasonal climate pattern, with most of the rainfall falling between
157 December and April (Lacroix et al. 2015), followed by a dry season. Annual rainfall amounts
158 range between 350 and 600 mm, with daily cumulative precipitation rarely exceeding 25 mm.



159 Numerous large landslides dot the Colca valley (Pham et al. 2018), often showing
160 retrogressive failure in the lacustrine deposits (Zerathe et al. 2016) and responding to
161 different trigger mechanisms (Lacroix et al. 2015, 2023; Bontemps et al. 2020). Persistent
162 uncertainties surround the factors controlling their evolution into slow or rapid landslides
163 (Zerathe et al. 2016), making the evaluation of their hazard potential difficult. Other landslides
164 in the valley that have been long creeping have been instrumented for years (Lacroix et al.
165 2014, 2015; Palmer 2017; Bontemps et al. 2020) , providing valuable insights into landslide
166 dynamics and responses to seismic and climatic triggers.

167 The Achoma landslide, failed catastrophically on 18th June 2020, unnoticed for a long time
168 until cracks were reported by locals in May 2020 (Dini et al. 2022; Lacroix et al. 2023), only
169 one month prior to failure. It is a large and deep-seated landslide that spans approximately
170 800 m in width along its scarp and extends 500 m downslope to the Colca River, covering an
171 area of about 0.4 km² (Figure 1). The headscarp rises approximately 100 m high (Lacroix et al.
172 2023), with estimated rupture surface depth averaging 50 m. The landslide volume is thus
173 estimated at around $20 \times 10^6 \text{ m}^3$.



Figure 1. Study area, Achoma landslide post failure (GoogleEarth Image, CNES/Airbus). Red rectangle in top left inset shows footprint of Sentinel 1 images (relative orbit number 47).

174 The failure occurred during the dry season, following cumulative rainfall of 600 mm during
175 the preceding wet season. Earlier findings indicated the landslide gradually accelerated three
176 months before its failure, initiating during the rainy season (Lacroix et al. 2023), suggesting
177 rainfall may have played a crucial role in the transition from slow to rapid movement. The site



178 has experienced seismic activity during the observation period, with the largest earthquake
179 recorded on 15th August 2016, measuring Mw 5.5 (Bontemps et al. 2020).

180

181 **3. Methods and data**

182 **3.1. Raw interferograms**

183 We generated 514 Sentinel-1 wrapped interferograms from 114 satellite acquisitions of
184 ascending track with relative orbit number 47, covering the period between 30th April 2015
185 and 20th June 2020 (the rupture of the Achoma landslide occurred the 18th of June) over the
186 Colca Valley, Peru. The interferograms were generated with the NSBAS processing chain (Doin
187 et al. 2011), at medium spatial resolution. Sentinel-1 data, originally acquired with a ground
188 resolution of 2.3 m in range and 14 m in azimuth, were multilooked (8 and 2 looks in range
189 and azimuth, respectively) to a final pixel size of 18.4 m × 28.2 m. Temporal baselines range
190 from 12 days (the minimum available for the area) to 1 year. The topographic contribution of
191 the signal was removed with the SRTM 30m digital elevation model. The interferograms were
192 not filtered, in order to avoid possible artefacts and loss of deformation signal (Strozzi et al.
193 2020).

194 A first inspection of the interferograms was carried out, this revealed a non-linear behaviour
195 of the landslide, characterised by phases of quiescence and activity. The nature of the
196 landcover, largely composed of agricultural land and the intermittent, occasionally strong
197 displacement gradients cause low coherence and low signal to noise (S/N) ratios in
198 interferograms with temporal baselines of 48 days and longer. The highest signal-to-noise
199 (S/N) ratios are observed for temporal baselines of 12 and 24 days. Thus, for the successive
200 analyses described in the following sections, we selected a series of 113 successive
201 interferograms with the shortest available baselines. Additionally, we included
202 interferograms with baselines of 30, 48, and 72 days to cover periods where shorter baselines
203 are unavailable due to missing images (Supplementary Figures 1-8). Whilst this approach does
204 not offer the redundancy of image connections required for time series inversion, it allows to
205 cover the observation window with the highest S/N ratio interferograms, whilst limiting the
206 number of gaps over the period.

207



208 The boundaries of the Achoma landslide were mapped in geographical coordinates based on
209 geomorphological characteristics observed on Google Earth optical images (Dini et al. 2022).
210 The polygon outline was then projected in the geometry of the radar images. The
211 interferograms were cropped around the landslide polygon, with the crop size (71 by 81
212 pixels) chosen to provide a margin around the landslide in each direction comparable in size
213 to the landslide itself. This allows for a meaningful comparison between the area inside the
214 landslide and the surroundings as well as for the presence of areas assumed stable (not
215 affected by displacements) and characterised by good temporal interferometric coherence
216 (equal to or higher than 0.4). A 5 x 5 pixels window was used to calculate coherence, γ , as:

$$\gamma = \frac{|\langle S_1 \cdot S_2^* \rangle|}{\sqrt{\langle S_1 \cdot S_1^* \rangle \langle S_2 \cdot S_2^* \rangle}} \quad (1)$$

218
219 where $\langle \cdot \rangle$ is the complex conjugation averaged over the chosen window and S_1 and S_2 are the
220 complex values of primary and secondary images composing an interferogram (Kumar and
221 Venkataraman 2011; Dini et al. 2022).

222
223 In the following sections, we illustrate: 1) the removal of the component of the phase signal
224 proportional to perpendicular baselines from the raw interferograms, to identify and mitigate
225 any residual component associated with topographic errors; 2) the analysis of coherence loss
226 patterns; 3) the analysis of the raw phase signal and its changes over time; and 4) the analysis
227 of the influence of seismicity, rainfall, and river erosion on the landslide's recent history.

228

229 3.2. Topographic error correction of raw interferograms

230 An area assumed stable (i.e., not affected by ground displacements) was chosen outside the
231 landslide boundaries. Various window sizes were tested for this area, and a 5 x 5 pixel window
232 was ultimately chosen—large enough to provide a more meaningful average of phase values
233 than a single pixel, yet small enough to avoid including areas with markedly different ground
234 reflectivity. The choice of the window was based on the average of a proxy of the temporal
235 coherence, as defined by Thollard et al. (2021), ensuring phase stability, this was followed by
236 a visual analysis of the geomorphological features in the proximity of the landslide. The phase
237 of each wrapped interferogram (prior to landslide failure) was referenced to the mean phase



238 of the selected stable reference window, $e^{i\varphi_{k,ref}}$, computed for each interferogram, k , by
239 multiplying the interferometric phase of all pixels by the complex conjugate of the average
240 phase within the reference window (Dini et al. 2022). After this referencing step, the influence
241 of the perpendicular baseline on the phase values of individual pixels within each
242 interferogram was analysed. Higher perpendicular baselines cause higher sensitivity to
243 topography (Colesanti and Wasowski 2006; Meyer and Sandwell 2012), therefore, if
244 topographic residuals exist after the topographic component removal with the SRTM digital
245 elevation model, a correlation between baselines and interferometric phase would be
246 revealed. Such topographic residual might be associated with low DEM accuracy or changes
247 of ground surface occurred after DEM acquisition and prior to SAR images acquisition. To do
248 this, we computed the average phase over 5×5 moving windows, l , over the entire crop,
249 noted $e^{i\varphi_{k,l}}$. To account for the circular nature of phase values (modulo 2π), a parameter
250 search was carried out to determine the best linear fit within the complex domain. For each
251 moving window, predicted values were calculated as:

$$e^{i\delta\varphi_{k,l}} = e^{iX_k\beta_l} \quad (2)$$

252 where $e^{i\delta\varphi_{k,l}}$ is the predicted phase in each window l of interferogram k , X_k is the
253 perpendicular baseline of each interferogram and β_l is the proportionality coefficient
254 between $e^{i\delta\varphi_{k,l}}$ and the perpendicular baseline for the window l (Dini et al. 2022). During the
255 parameter search, multiple bounds for β were tested before selecting -0.5 and 0.5 rad/m, with
256 a step size of 0.001. The value of β is determined by maximising the coherence ρ_k between
257 the predicted and observed values given by:

$$\rho_k = \left| \frac{\sum_k e^{i\varphi_{k,l}} * e^{i\delta\varphi_{k,l}*}}{N} \right| \quad (3)$$

259 where N is the number of interferograms (Dini et al. 2022). Maps of β , ρ and corrected
260 interferograms were generated. An example of the relationship between phase and
261 perpendicular baseline for all interferograms is shown in figure 2.

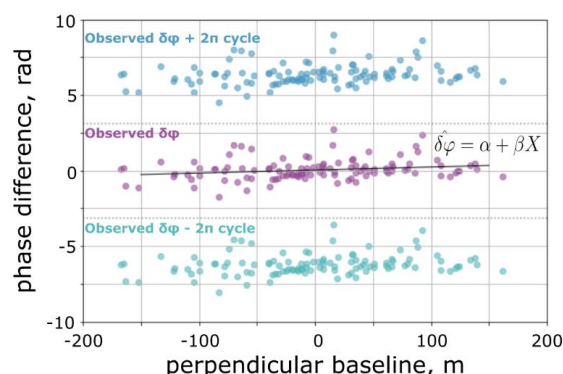


Figure 2. Example of correlation between phase and perpendicular baseline for one moving window. Each purple point represents the complex average phase in the sample window for a given interferogram with respect to the complex average phase in the reference area. As the phase is known in modulo 2π , its $+2\pi$ and -2π values are also shown in blue and teal respectively. (Modified from Dini et al. 2022, Gretsli Colloque Proceedings).

3.3. Coherence loss analysis

Interferometric coherence and its changes within the landslide and in the surrounding area were analysed both in space and time, in a qualitative and quantitative way respectively. We retained all the selected 113 successive interferograms for this analysis, irrespective of their average coherence. This is because if coherence is to be used as a precursory indicator, its potential should be tested over a range of interferograms, including those in which the phase might be unreliable. Spatial coherence loss is identified within individual interferograms. We focused on patterns of coherence loss over confined areas, as a proxy of localised strain: localised and spatially organised changes of the complex interferometric values are likely associated with localised displacements, particularly if these correspond to gravitational morphological features.

In order to detect changes in mean coherence through time and between the landslide and the surrounding gravitationally stable areas, we first calculated for each interferogram the average coherence over the whole crop, along the scarp and within the mapped landslide boundaries. The scarp and crown areas are key locations for precursory detection as motion related to retrogression might be focused here. Boundaries for the scarp were mapped on Google Earth optical images on the basis of geomorphological features and then converted in radar coordinates, as for the landslide boundaries. We analysed the average coherence time series in relation to daily rainfall, downloaded from the online platform of the national service



284 of Meteorology and Hydrology of Peru (Servicio Nacional de Meteorología e Hidrología del
285 Perú). We then computed the time series of the ratio between average landslide coherence
286 and average coherence of the surrounding area (Jacquemart and Tiampo 2021). The ratio is
287 chosen because it highlights changes occurring in the landslide with respect to the
288 surroundings, whilst accounting for periods of coherence loss associated to vegetation
289 changes or ground moisture changes due to rainfall events that would affect the coherence
290 everywhere in a similar way. The changes highlighted by such ratio are therefore most likely
291 associated with ongoing deformation inside the landslide area.

292

293 3.4. Wrapped phase analysis

294 As explained in section 1, the presence of interferograms with a high displacement gradient
295 and/or low S/N ratio hinders the ability to perform reliable phase unwrapping without errors
296 during phases of landslide acceleration. We thus adopted the following procedure to analyse
297 the wrapped phase signal in time, whilst avoiding phase unwrapping. Following an approach
298 similar to that presented in López-Quiroz et al. (2009), we selected 5 interferograms
299 characterised by high S/N ratio and by relatively low displacement gradients. In particular, we
300 ensured to select only interferograms in which the observed displacements gradients would
301 not exceed 2π over the landslide area. The visual inspection of all wrapped interferograms
302 revealed that the area affected by displacements has a similar spatial pattern until failure and
303 that the displacement gradient, as observed in interferograms with higher S/N ratio, has the
304 same sign throughout (which is expected in gravitational motion). For the five chosen
305 interferograms we added 2π to all pixels with phase value < -1 rad, thus obtaining a pattern
306 with values comprised between -1 and 5.28 rad. We then averaged these interferograms,
307 obtaining what we will refer as a model deformation pattern (Figure 3A). We cut the area
308 closely around the deformation pattern over 33 by 33 pixels, in order to reduce the
309 contribution of noise in the surrounding area. We then used this model pattern to investigate
310 its correlation with all 113 interferograms in the series, so that:

311

$$e^{i\widehat{\delta\varphi}_{k,p}} = e^{iM_p\alpha_k} \quad (4)$$

312

313 where $e^{i\widehat{\delta\varphi}_{k,p}}$ is the predicted phase value at pixel p of interferogram k , M_p is the phase value
314 of the model deformation pattern at pixel p and α_k is the proportionality coefficient between

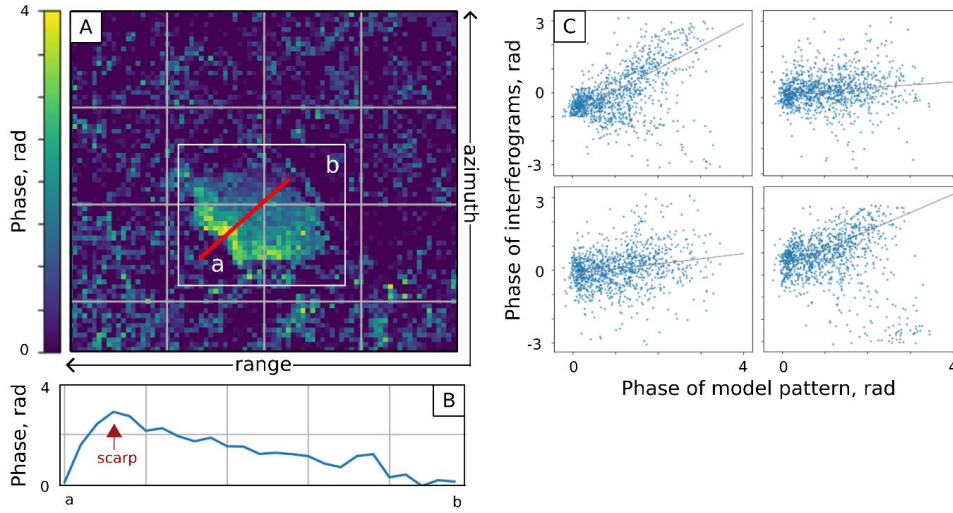


Figure 3. A) Model pattern of deformation in radar coordinates (flipped left-right); B) model pattern phase gradient for the profile a-b; C) examples of four interferograms showing the pixel-by-pixel correlation with the model pattern (from top left, clockwise: 18/08/2018-30/08/2018, 30/08/2018-11/09/2018, 23/09/2018-05/10/2018, 05-10/2018-29/10/2018).

the phase of the model pattern and interferogram k (Figure 3B). For the parameter search, -
7 and 7 were chosen as bounds for α_k , to account for potentially large displacements that
might have affected the landslide in the days/weeks before failure, with a 0.001 step. The
value of the proportionality coefficient α_k is then used to represent a dimensionless measure
of displacement rates, DI , which is a quantity of activity for each interferogram in the series.
For example, interferograms characterised by α_k around zero are those with no detectable
displacements, whilst α_k around 1 would indicate for interferogram k a similar displacement
gradient to the model pattern. The value of α_k is obtained by maximising the coherence
between the predicted and observed values, the latter a measure of the goodness of fit:

$$\gamma_k = \left| \frac{\sum_k e^{i\varphi_{k,p}} * e^{i\delta\varphi_{k,p}^*}}{N_p} \right| \quad (5)$$

where N_p is the number of pixels in interferogram k . Successively, the same procedure was
applied only to pixels falling within the landslide, masking outside pixels. This was done to
generate a ratio between the best coherence calculated over landslide pixels only and the
coherence over all pixels, including surrounding area pixels. A low ratio indicates poor fit of



330 the model within the landslide area in particular, which in turn indicates high likelihood of
331 high displacements gradients leading to spatial aliasing and decorrelation. A threshold of such
332 ratio was set at one standard deviation below the mean value. Unreliable interferograms
333 (grey dots in figure 5) are those with ratio falling below this threshold.

334

335 3.5. InSAR-derived downslope displacements

336 The dimensionless measure of displacement rates, DI , obtained with the analysis of raw phase
337 in successive interferograms described in section 2.4 is not an absolute measure of
338 displacements. It represents the degree of activity within the landslide in the time interval
339 covered by each interferogram, as it reflects the correlation between the model pattern and
340 each interferogram. Figure 3C shows a profile across the model that runs along the maximum
341 slope gradient roughly, through the middle of the landslide. The highest values are observed
342 at the scarp, with a maximum value, r_{max} , of 3.45 radians, decreasing to around zero at the
343 toe of the landslide. Therefore, to estimate line of sight (LOS) displacements in mm, we
344 rescaled the dimensionless displacement rates, DI , as:

345

$$DI_{mm} = DI * r_{max} * \frac{\lambda}{2\pi} \quad (6)$$

346

347 where λ is the half the wavelength of the satellite, which for Sentinel-1 is 28 mm.

348 An assumption generally accepted for landslides is that the displacement vector is oriented
349 along a line of maximum slope gradient (Notti et al. 2012). This reflects the overall motion of
350 the landslide, even if, unless the landslide is a pure translational slide, some parts of
351 compound landslides have higher vertical component of the displacements than others.
352 Following the approach presented in Notti et al. (2011), we computed a coefficient that
353 describes the percentage of downslope displacement that is detectable along the line of sight
354 and applied a correction to the displacements. This coefficient is 0.8, for an incidence angle
355 over the area of 40.7 degrees, a heading angle of 347 degrees, and average slope and aspect
356 of 20 degrees and 74 degrees respectively.

357 We then applied a correction to the displacements obtained with the optical image
358 correlation, DO , described in section 2.4, once again assuming that the displacements occur
359 along the maximum slope gradient and taking an average slope angle of 20 degrees, so that:

360



$$DO_{mm} = \frac{DO}{\sin(\vartheta)} \quad (7)$$

361

362 where ϑ is 70degrees, the complementary to the average slope angle.

363 Finally, we identified the onset of activity periods in the InSAR time series, we fitted for each
364 period a linear model. We then computed the slope of the curve for each phase and compared
365 the values at different ones.

366

367 3.6. External forcing

368 In order to detect external events that may have played a role in the onset of activity at
369 specific times, we took into consideration seismicity, rainfall and maximum river width as a
370 proxy for erosion. The pore pressure increase associated with rainfall (Carey et al. 2019;
371 Agliardi et al. 2020) and seismic shaking (Lacroix et al. 2022a) is an important factor that
372 perturbs the internal stress state of the rupture surface of large landslides, inducing slip onset
373 (Agliardi et al. 2020). River erosion also plays a role in modulating landslide activity in the
374 region (Lacroix et al. 2015) and increased fluvial erosion might increase landslide activity by
375 removing material at the toe (McColl 2022), undercutting the slope (Ballantyne 1986;
376 Fourniadis et al. 2007; Yang et al. 2021) and potentially exposing the sliding surface.

377

378 3.6.1. Earthquakes

379 We computed a comprehensive list of earthquakes with magnitude 3 and above, occurred
380 within a radius of 150 km of the Achoma landslide, between 2015 and July 2020 from the
381 online platform of the Geophysical Institute of Peru's (Instituto Geofísico del Peru). The list
382 comprises of 361 events. For each event, we calculated the expected peak ground
383 acceleration (PGA, m/s^2) as indicator of seismic ground motion at the Achoma landslide site
384 by applying the ground motion prediction method of Akkar and Bommer (2010). This method
385 was shown by previous studies to perform well for a landslide site located approximately 10
386 km west of the Achoma landslide (Lacroix et al. 2015; Bontemps et al. 2020). PGAs of $0.1 m/s^2$
387 and above are obtained for earthquakes occurred at less than 50 km from the landslide, with
388 magnitudes comprised between 3.8 and 5.6, except for one event, occurred at 84 km, but
389 with magnitude 6.2.

390

391



392 3.6.2. Rainfall

393 Hourly rainfall data starting from 2015 recorded at the station of Chivay, approximately 9 km
394 northeast of the landslide site, at a similar elevation, were downloaded from the online
395 platform of the National Service of Meteorology and Hydrology of Peru. This was then
396 converted into daily rainfall totals. Cumulative rainfall for each dry-rainy season sequence
397 (August to August of following year) has been plotted for every year, to compare activity rates
398 with rainfall. 2015 and 2016 were characterised by drier conditions than following years. To
399 identify more intense daily rainfall events, characterised by higher 24 hours cumulative
400 rainfall, we computed the histogram of daily rainfall, which presents a skewed right
401 distribution. We selected a threshold of 25 mm/day as the intense rainfall event, as
402 frequencies of higher daily totals do not exceed 1 in the whole observation period.

403

404 3.6.3. River erosion

405 As a proxy for river erosion at the landslide's toe, we analysed the changes in river width over
406 time. To accomplish this, we utilised 219 Planet Lab PlanetScope images with 3m ground
407 resolution. We selected three sections along the river: one in the middle of the landslide and
408 one at each boundary. For each image, we measured the river's width at each of the three
409 locations. The river's width broadly follows a seasonal pattern corresponding to the seasonal
410 rainfall over the area, implying that the river's erosive power follows a similar temporal
411 pattern to the rainfall. However, our objective was to identify unseasonably large river events
412 that might be triggered by localised events upstream in the catchment, which are not directly
413 recorded at the nearby meteorological station. To identify such unseasonable events, we
414 computed a rolling mean of the river width and looked for peaks exceeding one standard
415 deviation from the mean. In addition to this, we mapped the riverbanks at maximum width
416 for each year, to determine any position changes through time that might be indicative of
417 persistent, significant erosion.

418

419 **4. Results**

420 4.1. Spatial coherence features as long-term precursors

421 Interferometric coherence maps generated for all selected successive interferograms (see
422 section 2) exhibit distinct, consistent features over the observation period (figure 4). Notably,



low coherence lineaments appear intermittently up to 5 years before the landslide failure. These features manifest as narrow, rope-like structures located primarily along the scarp and southeastern flank of the landslide, consistent with post-failure observations. Interestingly, these features persist even in interferograms characterised by generally low coherence, where phase unwrapping would typically be unreliable. They are identifiable in 25 interferograms spanning from the earliest available (covering the period 30th April 2015 to 11th July 2015) up until 16th March 2020, approximately three months prior to the failure. Starting from 9th April 2020 the entire area affected by the landslide shows a more widespread loss of coherence, indicative of a regime shift.

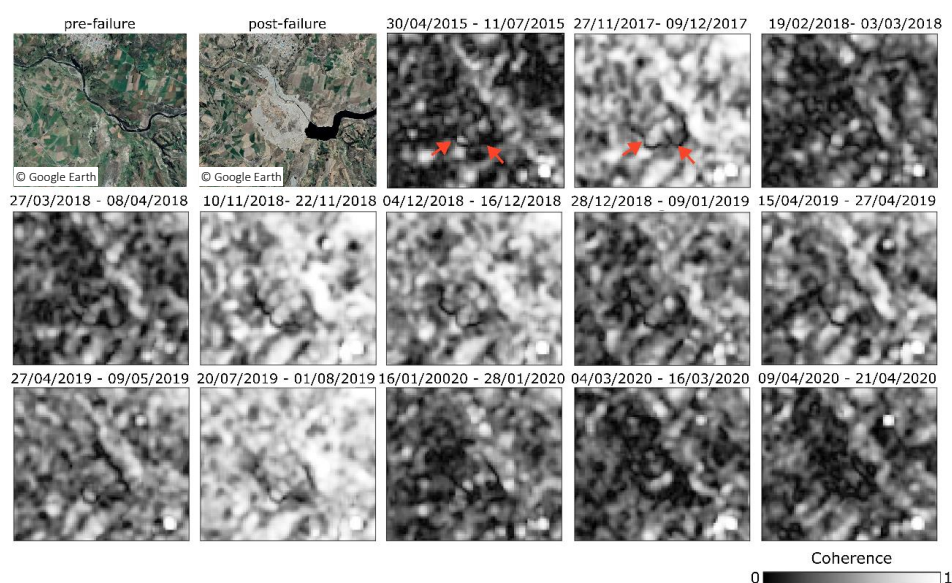


Figure 4. Pre- and post-failure Google Earth images with a series of interferometric coherence examples showing the development of headscarp and southern boundary, with the change in regime from March 2020.

4.2. Time series of coherence ratio

Figure 5A illustrates the average coherence in the landslide area and in the surrounding area. Albeit with some small differences, the coherence drops everywhere following similar temporal patterns during the rainy seasons. The coherence ratio between the landslide and the surrounding area (figure 5B) remains around 1, with a mean of 0.98, from 30th April 2015 to 28th March 2020, encompassing multiple wet seasons. Subsequently, starting from this



440 date until the failure on 18th June 2020, the ratio progressively declines below 0.8, reaching
441 its lowest value of 0.19 at the time of failure.

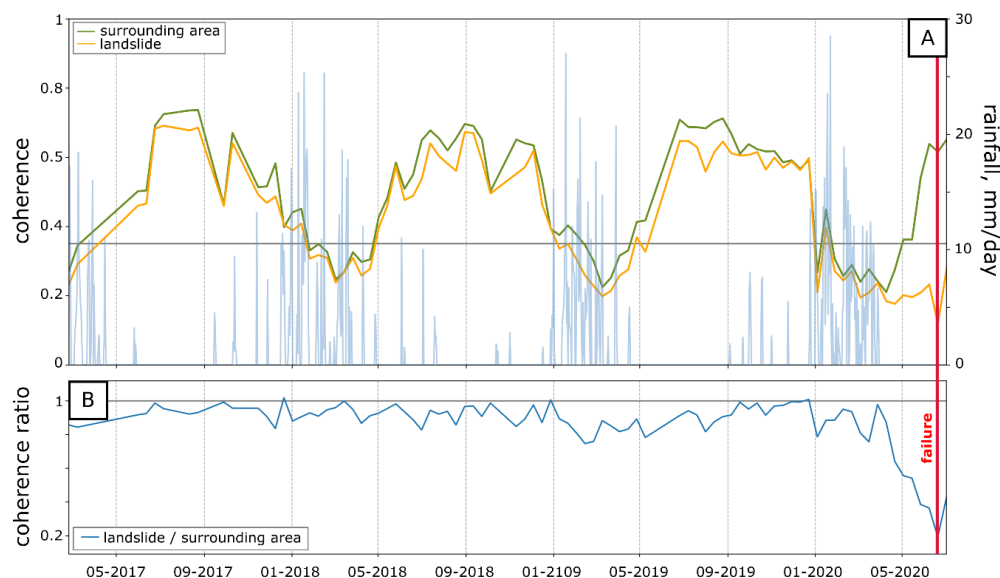


Figure 5. A) Interferometric coherence for different parts of the landslide, superposed on daily rainfall. B) Coherence ratio. Failure is indicated by the vertical red line.

442

443 4.3. Acceleration phases as seen by InSAR

444 The dimensionless activity index time series, derived using the method outlined in section 2.5,
445 is shown in figure 6. The time series reveals periods of relative stability interspersed with
446 phases of acceleration. Transient creep events are characterised by displacements occurring
447 within individual or, in one case, over two consecutive interferograms amid periods of
448 minimal long-term displacements. Four transient creep events between April 2015 and
449 August 2016 exhibit dimensionless displacement rates exceeding 1, occurring amidst a
450 backdrop of rates generally around 0 and less than 0.25 (Figure 6; Table 1). The displacements
451 observed in these interferograms match or exceed the mean deformation pattern shown in
452 figure 3A. In contrast, we observe long acceleration phases, periods during which
453 displacement rates increase significantly over three successive interferograms or more. These
454 become apparent from November 2017 onwards.



455 Four distinct acceleration phases are observed:

- 456 • Phase 1: 27th November 2017, to 8th April 2018
- 457 • Phase 2: 19th June 2018, to 9th May 2019
- 458 • Phase 3: 8th July 2019, to 20th July 2019
- 459 • Phase 4: 4th January 2020, to 4th March 2020 (culminating in failure 3 months later)

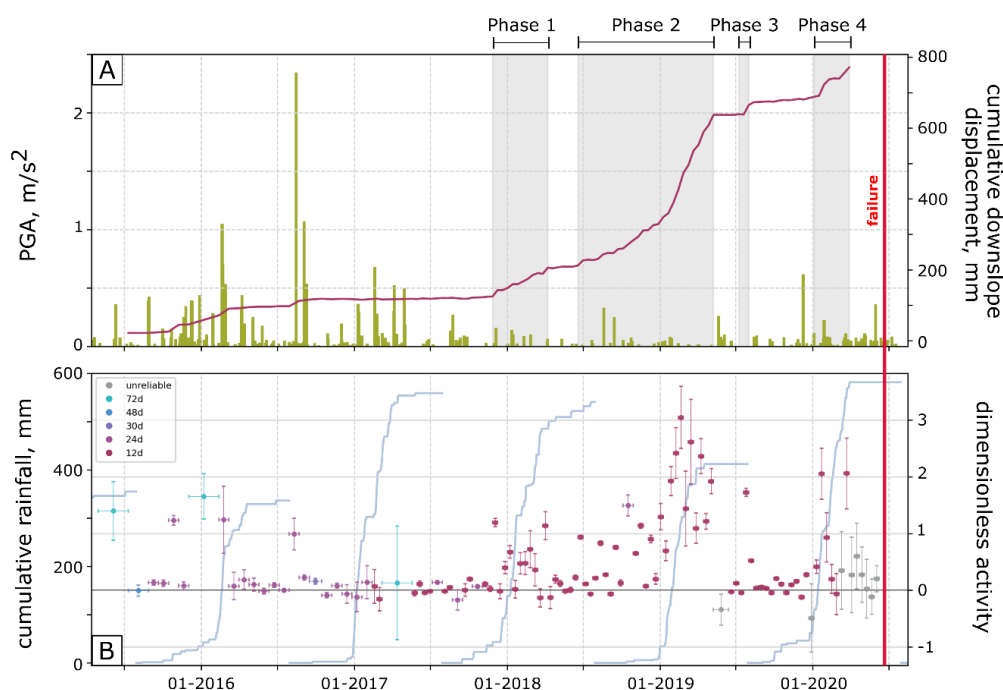


Figure 6. A) purple curve, estimated downslope cumulative displacement in mm after correction; green bars, PGA. B) dimensionless activity index, every dot represents an interferogram, different colours and horizontal bars represent interferogram duration, vertical bars $1/\gamma_k$ normalised by its max value (eq 5); blue curves, cumulative rainfall over the rainy season.

460 The accelerations are detected using the dimensionless index (see section 2.4), but we
 461 present below the estimated rates (see section 2.5), for ease of description.

462 The first acceleration begins with an initial significant displacement (~18 mm in 12 days),
 463 followed by a period of linear displacements over 132 days at an almost steady rate of
 464 approximately 279 mm/year.



465 The second phase follows a 10-week quiescence period and exhibits escalating trends: 234
466 mm/year between 19th June 2018, and 5th October 2018; 425 mm/year between 5th October
467 2018, and 9th January 2019; and 1080 mm/year between 9th January 2019, and 9th May 2019.
468 A short acceleration in July 2019 transitions quickly into a brief period stability followed by a
469 phase of low, steady-rate creep from 1st August 2019 to 23rd December 2019, characterised
470 by a gentle trend of 38 mm/year. This is succeeded by the last acceleration phase, reaching
471 approximately 567 mm/year from 4th January 2020 to 4th March 2020, the last reliable
472 interferogram captured, then culminating in failure.

473

474 **5. Discussion**

475 **5.1. Spatial patterns of low coherence**

476 The coherence maps derived from successive interferograms reveal slope instability by
477 delineating gravitational morphological structures dating back five years before failure. In the
478 earliest available interferogram (30th April 2015 – 11th November 2015), a distinct low
479 coherence boundary is evident despite the low average coherence, closely mirroring the later
480 spatial development of the landslide. The low-coherence markers likely indicate areas of
481 strain resulting from landslide displacement, marking the boundary between stable and
482 unstable ground. These markers are interpreted as early signs of destabilisation, suggesting
483 strain concentration along the failure surface is beginning to occur, albeit with very small
484 displacements. We observed similar features in other landslides in the Colca Valley, indicating
485 that these signals are not isolated occurrences and highlighting their importance and
486 reliability for early detection at large scales. Some of these landslides have exhibited long-
487 term creep without progressing to catastrophic failure. In these cases, low-coherence
488 markers appear to indicate retrogressive behaviour with the formation of secondary scarps
489 over the years and delimiting different activity sectors.

490

491 **5.2. Factors influencing coherence loss**

492 Low interferometric coherence, reflecting high phase variability between adjacent pixels, can
493 be caused by factors like dense vegetation, crops, surface debris, snow, or spatial
494 heterogeneity of ground deformation. In the case of the Achoma landslide, the low coherence
495 markers observed are unlikely to be caused by localised land cover changes. Instead, they



likely reflect slight differential displacements associated with the development of surface discontinuities. These features have been observed up to three months before failure, similar to the final acceleration stage detected with optical images by Lacroix et al. (2023). Jacquemart et al. (2021) discuss various factors contributing to interferometric coherence loss in landslides, including soil moisture changes, erosion, vegetation dynamics, and active slope deformation. While distinguishing between these causes is challenging, their combined presence suggests increased landslide activity.

The observed transition in coherence patterns, from localised anomalies along gravitational structures to widespread loss across the entire landslide area in March 2020, points to significant shift in landslide dynamics. This likely marks the transition from small displacements (with the landslide behaving as a cohesive body) to higher displacement gradients and internal deformation. Identifying such transitions in coherence could provide valuable lead time for early warnings, offering a proactive approach to landslide monitoring in previously unmonitored areas.

510

5.3. Coherence ratio analysis

In addition to the spatial patterns of low coherence, we analysed the ratio between the mean coherence over the landslide area and that in the surrounding area, using a methodology similar to that adopted by Jacquemart and Tiampo (2021). This ratio helps account for temporal coherence variability that affects both the landslide and its surroundings similarly. For example, seasonal moisture changes can impact coherence, but the ratio remains close to 1 unless changes occur specifically within the landslide area.

A noticeable drop in the coherence ratio occurred approximately three months before the failure event, beginning around 4th March 2020. By setting a retrospective threshold (one standard deviation below the mean coherence ratio), we identified that this threshold was surpassed between 9th and 21st April 2020, indicating predictive value about two months before the Achoma failure. Jacquemart and Tiampo (2021) noted a similar coherence ratio decline approximately five months before the Mudcreek landslide, attributing it partly to vegetation degradation. In contrast, our analysis of the Achoma landslide shows a sharp increase in the coherence ratio post-failure, reaching values as high as 1.98 during the 2021 rainy season. This increase suggests that vegetation degradation following the failure may expose rock and soil, enhancing phase stability in the absence of displacements. Thus, the



528 observed drop in coherence leading up to failure is likely associated with high displacement
529 gradients leading to increased internal deformation of the landslide mass and phase aliasing.
530 This observation is consistent with the three-month final acceleration stage identified
531 through independent measurements by Lacroix et al. (2023). Further investigation into other
532 case studies is needed to establish universal indicators and thresholds for landslides at critical
533 stages.

534

535 5.4. Dimensionless activity index

536 The InSAR data processed in this work indicates that the Achoma landslide underwent a long
537 evolution. Our observations show that progressive damage and fault maturation over a
538 period of at least five years, likely longer, ultimately led to landslide failure, in agreement with
539 the findings of Lacroix et al. (2023). To simplify, we separately discuss two broad periods,
540 based on different styles of activity observed.

541

542 *April 2015 to December 2017*

543 The key observation is that between April 2015 and December 2017 the long-term activity
544 index for this period reveals short-lived transient creep events in response to perturbations,
545 interspersed with prolonged period of little to no activity (Figure 6; Table 1). This suggests the
546 presence at this stage of a maturing surface of rupture, allowing for some hydro-mechanical
547 fluid-solid coupling (Agliardi et al. 2020), but not yet a self-sustaining process of progressive
548 failure. Displacements during this period may span up to 72 days due to sampling intervals.
549 Between December 2015 and March 2016, a combination of moderate seismicity and rainfall
550 led to possible prolonged displacements over two consecutive interferograms for up to 96
551 days. However, the temporal resolution of the data does not allow us to determine whether
552 movement was continuous or intermittent within these intervals.

553 While the August 2016 earthquake, with the highest PGA of 2.34 m/s^2 recorded during the
554 study period, did result in some movement, it was lower than the movements observed
555 between April 2015 and March 2016. Moreover, although the rainy season of 2016/2017
556 recorded comparable precipitation totals to subsequent seasons, no prolonged period of
557 acceleration was observed until the end of 2017. This suggests that a combination of
558 seismicity and rainfall may be more critical for driving significant acceleration than either
559 factor alone. Unlike the Maca landslide, which exhibited prolonged post-seismic accelerations



560 following the 20 February and 15 August 2016 earthquakes, lasting 5 months and several
561 weeks, respectively (Bontemps et al. 2020), the Achoma landslide's response was transient
562 and not sustained, as no subsequent interferograms indicated continued movement. Post-
563 seismic motion has been associated to pore-water pressure increases due to sediment
564 contraction (Lacroix et al. 2022a). The absence of post-seismic motion at the Achoma landslide
565 may reflect that the rupture surface was not sufficiently mature, and lacked the necessary
566 pathways for water to migrate from contracted sediments to the rupture zone. Without this
567 migration, the pore pressure at the rupture surface could not build up to a level that would
568 sustain post-seismic motion.

569

Interferogram dates (and duration in days)	Max PGA m/s ²	Number seismic events	Dimensionless displacement (estimate mm)	Estimate displacement rate mm/yr	Cumulative rainfall mm
30/04/2015 – 11/07/2015 (72)	0.36	6	1.4 (~26)	~132	9.1
15/10/2015 – 08/11/2015 (24)	0.15	4	1.2 (~23)	~350	13.1
02/12/2015 – 12/02/2016 (72)	0.44	26	1.7 (~31)	~157	56.4
12/02/2016 – 07/03/2016 (24)	1.05	9	1.2 (~23)	~350	160.1
29/07/2016 – 22/08/2016 (24)	2.34	7	1 (~18)	~274	0

570 **Table 1.** Interferograms showing possible transient creep behaviour associated with nearby earthquakes.

571

572

573 *December 2017 to June 2020*

574 A shift in behaviour can be identified from December 2017: from this point, longer periods of
575 activity begin to occur. The landslide reacts quickly to the onset of the wet season in
576 December 2017, despite lower seismicity than in the previous period, suggesting that the
577 rupture surface has fully developed and become more sensitive to perturbations. This likely
578 reflects the formation of a fine-grained gouge along the basal shear plane (Agliardi et al.
579 2020), reducing permeability and altering pore pressure dynamics. These internal changes led
580 to cycles of acceleration, deceleration, and steady-state stages (Zhou et al. 2018) (Figure 6A),
581 driven by transient perturbations like seismic events or rainfall and modulated by
582 mechanisms like pore pressure dissipation (Lacroix et al. 2022b) or strain-strengthening
583 behaviour (Agliardi et al. 2020) ultimately resulting in sustained slip rates even during dry
584 periods. This pattern is particularly evident during the dry season of 2018, when the Achoma
585 landslide exhibited sustained displacement rates despite the absence of significant external
586 triggers. This observation highlights the role of ongoing internal processes, such as continued



587 damage accumulation along the basal shear plane, in maintaining instability and movement
588 over time.

589 As Lacroix et al. (2023) note, the final stage of acceleration began in the wet season. While
590 optical images from Lacroix et al. (2023) pinpoint the beginning of the final acceleration in
591 March 2020, InSAR-based observations in this study suggest that the landslide began
592 accelerating as early as January 2020, following a period of steady slip rates during 2019.
593 Although rainfall was undoubtedly a key factor, similar rainfall totals in 2017 and 2018 did not
594 lead to failure, suggesting that other factors, such as accumulated damage or changes in the
595 basal shear zone, were more critical in 2020. Increased seismic activity in the final stages,
596 marked by a higher frequency of smaller earthquakes, likely contributed to the landslide's
597 acceleration, demonstrating a combination of driving factors.

598

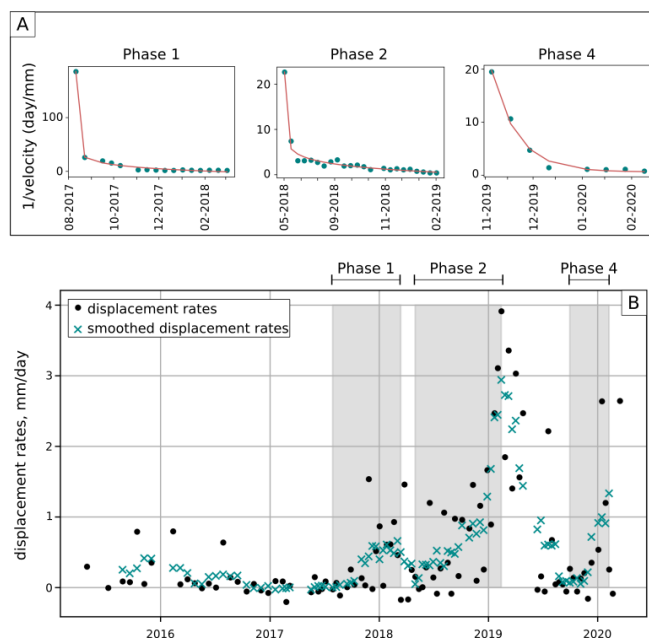


Figure 7. A) $1/\text{velocity}$ plots for phase 1, phase 2, and phase 3. B) Displacement rates for raw (black dots) and smoothed data (blue x, smoothed using a 5-window running mean). Shaded areas show accelerations of phase 1, phase 2 and phase 4.

599 Figure 8 shows phases of accelerations 1, 2, and 4 plotted as inverse velocity (day/mm),
600 calculated from estimated displacements, with asymptotic decay indicating the attainment of
601 steady states (Carlà et al. 2017b). Although external forcing factors, such as rainfall and
602 seismic events, inevitably modulated the landslide's response, our observations show that



603 they alone cannot explain the observed behaviour. For instance, comparable rainfall totals
604 than those in 2019-2020 did not cause failure, and acceleration continued through the 2018
605 dry season. The $1/v$ plots highlight the gradual internal process of material degradation,
606 through microcrack formation and coalescence, leading to the development of a shear
607 surface by March 2020. This combination of fluctuating external factors and internal
608 degradation explains the landslide behaviour prior to failure. By observing behaviour linked
609 to progressive failure, we demonstrate how dimensionless parameters from the wrapped
610 phase can be invaluable for long-term monitoring of such mechanisms, offering the potential
611 for significant lead times.

612

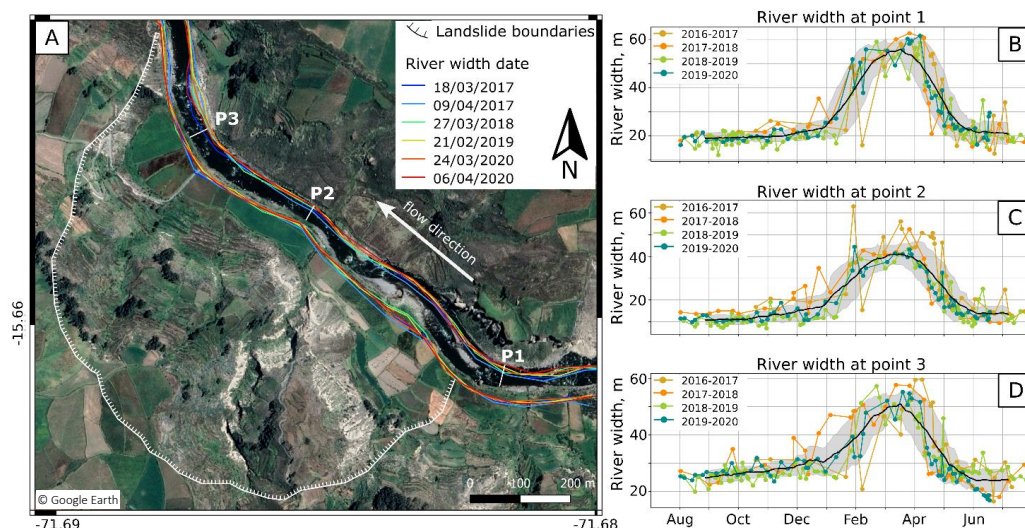


Figure 8. A) Mapping of riverbanks position at maximum width. If date of maximum width differs between P1, P2, P3, multiple dates per wet season are taken (e.g. 2017, 2020). Mapping and annotations are superposed to a Google Earth pre-failure satellite image. B-D) River widths for P1, P2, P3 respectively. Data is plotted from dry season to dry season the following year. The black curve represents the 40-day running mean, and the grey shading represents one standard deviation above and below the mean.

613 Figure 7A shows the position of the riverbanks during maximum river width periods for each
614 wet season (2016–2020). Despite potential image resolution limitations, our observations
615 reveal no clear trend of significant erosion toward the left bank or landslide toe. Instead,
616 riverbank positions vary over time, indicating movement in both directions, into and away
617 from the landslide toe. The right bank shows a slight tendency to move away, possibly due to
618 the landslide toe pushing the riverbed, which may increase erosion on that side. River width
619 measurements in Figure 7B-D, used as a proxy for erosional power, do not indicate significant



erosion events during the 2020 dry season. These findings suggest that the landslide was not triggered by high river erosion, but rather by a long-term process of progressive failure.

5.5. Complementarity

Our observations highlight variations in the Achoma landslide's response to triggers, depending on its stage of basal shear plane maturation, suggesting that different processes were involved. We retrospectively identify the beginning of a final acceleration already in January 2020 (as shown by wrapped phase dimensionless activity marker), transitioning into a critical and irreversible instability in March 2020 (as shown by coherence both in space and time), indicating that proactive monitoring could have commenced at least at this critical stage. This finding echoes Jacquemart and Tiampo's (2021) observation of a coherence ratio drop five months before the failure of the Mudcreek landslide, emphasising its potential as early indicator. They also noted that an approach based on time series generation underestimated displacements. In contrast, Handwerger et al. (2019) used a preprocessing step for signal removal before unwrapping in their analysis of the same landslide. Our method, leveraging wrapped phase analysis, offers a more streamlined alternative, providing valuable insights into landslide evolution without complex preprocessing. Unlike traditional InSAR approaches requiring signal removal and reintroduction, our method is less time-consuming and demonstrates the effectiveness of analysing the wrapped phase. In addition to this, integrating InSAR-based signals with optical time series enhances the understanding of landslide dynamics across different phases. The metrics we propose identify areas of incipient strain and early acceleration phases, while optical time series capture the final acceleration phase characterised by larger displacements (Supplementary figure 9).

The indicators proposed here rely on the identification of critical features, such as gravitational structures in the coherence signal or the moving mass in the wrapped phase. Automated detection of these features using machine learning techniques could significantly enhance landslide monitoring. Approaches such as that proposed by Chen et al. (2022) demonstrate the feasibility of applying deep semantic segmentation to recognise active landslides from InSAR. Implementing similar AI-driven frameworks on the precursors identified here could automate the detection of early instability signs, reducing reliance on



650 manual interpretation and providing an efficient first filter for identifying destabilising slopes
651 across large areas.

652

653

654 **6. Conclusions**

655 Using Sentinel-1 interferograms with non-overlapping short temporal baselines, we identified
656 precursors to the Achoma landslide. Our approach bypasses traditional unwrapping and time
657 series generation, revealing significant spatial coherence loss that indicates gravitational fea-
658 tures linked to strain localization along the rupture surface, visible five years prior to failure.
659 Intermittent coherence loss from approximately five years to five months before failure sug-
660 gests the progressive development of a hydro-mechanically coupled rupture surface with in-
661 creasing damage concentration. This is further supported by the acceleration, steady-state,
662 and deceleration phases observed in the wrapped phase analysis. Our findings demonstrate
663 the potential of satellite-based InSAR to detect destabilisation precursors before large dis-
664 placements occur, particularly when continuous displacement time series are hindered by
665 land cover or landslide behaviour. By integrating key parameters and their spatiotemporal
666 changes, this methodology could enhance the identification of precursors over larger areas
667 than traditional time series methods alone, making satellite-based monitoring even more val-
668 uable for landslide prediction. However, further research across a broader range of case stud-
669 ies is needed to validate coherence loss patterns as reliable precursors for landslides with
670 minimal ground displacement.

671 Our findings are significant for two practical reasons. First, the Achoma landslide went unno-
672 ticed until shortly before failure, a common issue in landslide science where monitoring typi-
673 cally begins after events occur rather than during early precursor stages. Identifying reliable
674 precursors in satellite data could improve landslide prediction on both local and broader
675 scales. Second, the challenge of monitoring landslides only after failure limits the capture of
676 earlier instability phases. Proactively targeting destabilising slopes for instrumentation is crit-
677 ical for effective hazard assessment, failure prediction, and understanding underlying pro-
678 cesses. A complementary approach that combines the strengths of InSAR and optical time
679 series, while leveraging AI for automated feature detection, holds remarkable potential for



680 advancing real-time landslide monitoring. Such innovations are key for mitigating hazards and
681 enhancing the resilience of vulnerable communities in landslide-prone regions

682

683

684

685 **Statements and Declarations**

686

687 **Authors Contribution**

688 BD conceived the idea submitted for CNES fellowship application, PL and MPD helped shape
689 the research. PL brought previous knowledge for the case study and contributed to concep-
690 tual ideas. BD and MPD designed the method for InSAR-based precursors. BD generated the
691 codes and carried out the analysis. BD, PL and MPD contributed to interpretation. BD wrote
692 the manuscript, PL and MPD provided critical feedback.

693

694 **Funding**

695 This study was carried out as part of a 2-year CNES funded fellowship to Benedetta Dini. The
696 fellowship was undertaken at ISTerre (Universite Grenoble-Alpes)

697

698 **Competing Interest**

699 The authors declare no competing interests.

700

701 **Data availability**

702 All the data used in this work is available from the original sources. Sentinel-1 data is freely
703 available at <https://browser.dataspace.copernicus.eu/>. Rainfall data is available at
704 <https://www.gob.pe/senamhi>. Seismic data is available at <https://www.gob.pe/igp>. PlanetLab
705 PlanetScope images are available at <https://www.planet.com/>. The codes written by the cor-
706 responding author to perform the analyses described in the methods could be made available
707 upon request.

708



709 References

- 710 Agliardi F, Scuderi MM, Fusi N, Collettini C (2020) Slow-to-fast transition of giant creeping
711 rockslides modulated by undrained loading in basal shear zones. *Nat Commun* 11:1–11
712 Akkar S, Bommer JJ (2010) Empirical equations for the prediction of PGA, PGV, and spectral
713 accelerations in Europe, the mediterranean region, and the Middle East. *Seismol Res Lett*
714 81:195–206. <https://doi.org/10.1785/gssrl.81.2.195>
715 Badoux A, Graf C, Rhyner J, et al (2009) A debris-flow alarm system for the Alpine Illgraben
716 catchment: design and performance. *Nat hazards* 49:517–539
717 Ballantyne CK (1986) Landslides and slope failures in Scotland: A review. *Scott Geogr Mag*
718 102:134–150. <https://doi.org/10.1080/00369228618736667>
719 Berardino P, Fornaro G, Lanari R, Sansosti E (2002) A new algorithm for surface deformation
720 monitoring based on small baseline differential SAR interferograms. *IEEE Trans Geosci*
721 *Remote Sens* 40:2375–2383
722 Bontemps N, Lacroix P, Larose E, et al (2020) Rain and small earthquakes maintain a slow-
723 moving landslide in a persistent critical state. *Nat Commun* 11:1–10.
724 <https://doi.org/10.1038/s41467-020-14445-3>
725 Carey JM, Massey CI, Lyndsell B, Petley DN (2019) Displacement mechanisms of slow-moving
726 landslides in response to changes in porewater pressure and dynamic stress. *Earth Surf*
727 *Dyn* 7:707–722
728 Carlà T, Intrieri E, Di Traglia F, et al (2017a) Guidelines on the use of inverse velocity method
729 as a tool for setting alarm thresholds and forecasting landslides and structure collapses.
730 *Landslides* 14:517–534
731 Carlà T, Intrieri E, Raspini F, et al (2019) Author Correction: Perspectives on the prediction of
732 catastrophic slope failures from satellite InSAR (*Scientific Reports*, (2019), 9, 1, (14137),
733 10.1038/s41598-019-50792-y). *Sci Rep* 9:1–9. <https://doi.org/10.1038/s41598-019-55024-x>
734
735 Carlà T, Macciotta R, Hendry M, et al (2017b) Displacement of a landslide retaining wall and
736 application of an enhanced failure forecasting approach.
737 <https://doi.org/10.1007/s10346-017-0887-7>
738 Chen X, Yao X, Zhou Z, et al (2022) DRs-UNet: A Deep Semantic Segmentation Network for the
739 Recognition of Active Landslides from InSAR Imagery in the Three Rivers Region of the
740 Qinghai–Tibet Plateau. *Remote Sens* 14:. <https://doi.org/10.3390/rs14081848>
741 Colesanti C, Wasowski J (2006) Investigating landslides with space-borne Synthetic Aperture
742 Radar (SAR) interferometry. *Eng Geol* 88:173–199
743 Cook KL, Rekapalli R, Dietze M, et al (2021) Detection and potential early warning of
744 catastrophic flow events with regional seismic networks. *Science* (80-) 374:87–92.
745 <https://doi.org/10.1126/science.abj1227>
746 Costantini M, Minati F, Trillo F, et al (2021) European Ground Motion Service (EGMS). In: 2021
747 IEEE International Geoscience and Remote Sensing Symposium IGARSS. pp 3293–3296
748 Dini B, Doin M-P, Lacroix P, Gay M (2022) Satellite-based InSAR: application and signal
749 extraction for the detection of landslide precursors, in: *Proceedings of 28th Colloque*
750 *Gretsi*, Nancy, France, 6-9 September 2022, 001-0308, p. 1233-1236
751 Dini B, Manconi A, Loew S (2019) Investigation of slope instabilities in NW Bhutan as derived
752 from systematic DInSAR analyses. *Eng Geol* 259:..
753 <https://doi.org/10.1016/j.enggeo.2019.04.008>
754 Dini B, Manconi A, Loew S, Chopel J (2020) The Punatsangchhu-I dam landslide illuminated
755 by InSAR multitemporal analyses. *Sci Rep* 10:8304



- 756 Doin M-P, Guillaso S, Jolivet R, et al (2011) Presentation of the small baseline NSBAS
757 processing chain on a case example: The Etna deformation monitoring from 2003 to
758 2010 using Envisat data. In: Proceedings of the Fringe symposium. ESA SP-697, Frascati,
759 Italy, pp 3434–3437
- 760 Fan X, Xu Q, Liu J, et al (2019) Successful early warning and emergency response of a
761 disastrous rockslide in Guizhou province, China. *Landslides* 16:2445–2457
- 762 Ferretti a, Prati C, Rocca F, et al (2005) Permanent Scatterers technology: a powerful state of
763 the art tool for historic and future monitoring of landslides and other terrain instability
764 phenomena. *Int Conf Landslide Risk Manag 18th Annu Vancouver Geotech Soc Symp* 1–
765 9
- 766 Ferretti A, Fumagalli A, Novali F, et al (2011) A New Algorithm for Processing Interferometric
767 Data-Stacks: SqueeSAR. *IEEE Trans Geosci Remote Sens* 49:3460–3470.
768 <https://doi.org/10.1109/TGRS.2011.2124465>
- 769 Ferretti A, Prati C, Rocca F (2001) Permanent scatterers in SAR interferometry. *IEEE Trans*
770 *Geosci Remote Sens* 39:8–20
- 771 Fiolleau S, Jongmans D, Bièvre G, et al (2020) Seismic characterization of a clay-block rupture
772 in Harmalière landslide, French Western Alps. *Geophys J Int* 221:1777–1788
- 773 Fourniadis IG, Liu JG, Mason PJ (2007) Regional assessment of landslide impact in the Three
774 Gorges area, China, using ASTER data: Wushan-Zigui. *Landslides* 4:267–278.
775 <https://doi.org/10.1007/s10346-007-0080-5>
- 776 Froude MJ, Petley DN (2018) Global fatal landslide occurrence from 2004 to 2016. *Nat Hazards*
777 *Earth Syst Sci* 18:2161–2181
- 778 Guzzetti F (2021) Invited perspectives: Landslide populations—can they be predicted? *Nat*
779 *Hazards Earth Syst Sci* 21:1467–1471
- 780 Handwerger AL, Huang M, Fielding EJ, et al (2019) OPEN A shift from drought to extreme
781 rainfall drives a stable landslide to catastrophic failure. 1–12.
782 <https://doi.org/10.1038/s41598-018-38300-0>
- 783 Instituto Geofísico del Peru Instituto Geofísico del Peru. <https://www.gob.pe/igp>. Accessed 1
784 Sep 2022
- 785 Intrieri E, Raspini F, Fumagalli A, et al (2018) The Maoxian landslide as seen from space:
786 detecting precursors of failure with Sentinel-1 data. *Landslides* 15:123–133
- 787 Jacquemart M, Tiampo K (2021) Leveraging time series analysis of radar coherence and
788 normalized difference vegetation index ratios to characterize pre-failure activity of the
789 Mud Creek landslide, California. *Nat Hazards Earth Syst Sci* 21:629–642.
790 <https://doi.org/10.5194/nhess-21-629-2021>
- 791 Kumar V, Venkataraman G (2011) SAR interferometric coherence analysis for snow cover
792 mapping in the western Himalayan region. *Int J Digit Earth* 4:78–90.
793 <https://doi.org/10.1080/17538940903521591>
- 794 Lacroix P, Berthier E, Maquerhua ET (2015) Earthquake-driven acceleration of slow-moving
795 landslides in the Colca valley, Peru, detected from Pléiades images. *Remote Sens Environ*
796 165:148–158. <https://doi.org/10.1016/j.rse.2015.05.010>
- 797 Lacroix P, Bièvre G, Pathier E, et al (2018) Use of Sentinel-2 images for the detection of
798 precursory motions before landslide failures. *Remote Sens Environ* 215:507–516.
799 <https://doi.org/10.1016/j.rse.2018.03.042>
- 800 Lacroix P, Dini B, Cheaib A (2021) Measuring kinematics of slow-moving landslides from
801 satellite images. In: *Displacement measurement by remote sensing Imagery*, Iste-Wiley.
802 London



- 803 Lacroix P, Gavillon T, Bouchant C, et al (2022a) SAR and optical images correlation illuminates
804 post-seismic landslide motion after the Mw 7.8 Gorkha earthquake (Nepal). *Sci Rep*
805 12:6266
- 806 Lacroix P, Gavillon T, Bouchant C, et al (2022b) SAR and optical images correlation illuminates
807 post-seismic landslide motion after the Mw 7.8 Gorkha earthquake (Nepal). *Sci Rep*
808 12:1–13. <https://doi.org/10.1038/s41598-022-10016-2>
- 809 Lacroix P, Huanca J, Angel LA, Taipei E (2023) Precursory Motion and Time-Of-Failure
810 Prediction of the Achoma Landslide, Peru, From High Frequency PlanetScope Satellites.
811 *Geophys Res Lett* 50:1–11. <https://doi.org/10.1029/2023GL105413>
- 812 Lacroix P, Perfettini H, Taipei E, Guillier B (2014) Coseismic and postseismic motion of a
813 landslide: Observations, modeling, and analogy with tectonic faults. *Geophys Res Lett*
814 41:6676–6680. <https://doi.org/10.1002/2014GL061170>
- 815 Li M, Zhang L, Ding C, et al (2020) Retrieval of historical surface displacements of the Baige
816 landslide from time-series SAR observations for retrospective analysis of the collapse
817 event. *Remote Sens Environ* 240:111695. <https://doi.org/10.1016/j.rse.2020.111695>
- 818 Liu P, Li Z, Hoey T, et al (2013) Using advanced InSAR time series techniques to monitor
819 landslide movements in Badong of the Three Gorges region, China. *Int J Appl Earth Obs*
820 *Geoinf* 21:253–264
- 821 Loew S, Gschwind S, Gischig V, et al (2017) Monitoring and early warning of the 2012 Preonzo
822 catastrophic rockslope failure. *Landslides* 14:141–154
- 823 Manconi A (2021) How phase aliasing limits systematic space-borne DInSAR monitoring and
824 failure forecast of alpine landslides. *Eng Geol* 287:106094
- 825 McColl ST (2022) *Landslide causes and triggers*. Elsevier Inc.
- 826 Meyer FJ, Sandwell DT (2012) SAR interferometry at Venus for topography and change
827 detection. *Planet Space Sci* 73:130–144.
828 <https://doi.org/https://doi.org/10.1016/j.pss.2012.10.006>
- 829 Notti D, Meisina C, Zucca F, Colombo A (2012) Models to predict Persistent Scatterers data
830 distribution and their capacity to register movement along the slope. *Proc FRINGE 2011*
831 2011:19–23
- 832 Palmer J (2017) Creeping catastrophes: Studies of slow landslides could unmask the
833 mechanics of a worldwide scourge. *Nature* 548:384–386.
834 <https://doi.org/10.1038/548384a>
- 835 Petley D (2012) Global patterns of loss of life from landslides. *Geology* 40:927–930
- 836 Pham MQ, Lacroix P, Doin MP (2018) Sparsity optimization method for slow-moving landslides
837 detection in satellite image time-series. *IEEE Trans Geosci Remote Sens* 57:2133–2144
- 838 Roy P, Martha TR, Khanna K, et al (2022) Time and path prediction of landslides using InSAR
839 and flow model. *Remote Sens Environ* 271:112899.
840 <https://doi.org/10.1016/j.rse.2022.112899>
- 841 Servicio Nacional de Meteorología e Hidrología del Perú Servicio Nacional de Meteorología e
842 Hidrología del Perú. <https://www.gob.pe/senamhi>. Accessed 10 Oct 2023
- 843 Strozzi T, Caduff R, Jones N, et al (2020) Monitoring rock glacier kinematics with satellite
844 synthetic aperture radar. *Remote Sens* 12:1–24. <https://doi.org/10.3390/rs12030559>
- 845 Strzabala K, Cwiakala P, Puniach E (2024) Identification of Landslide Precursors for Early
846 Warning of Hazards with Remote Sensing. *Remote Sens* 16:.
847 <https://doi.org/10.3390/rs16152781>
- 848 Thollard F, Clesse D, Doin M-P, et al (2021) FLATSIM: The ForM@Ter Large-Scale Multi-
849 Temporal Sentinel-1 InterferoMetry Service. *Remote Sens.* 13



- 850 Thouret JC, Wörner G, Gunnell Y, et al (2007) Geochronologic and stratigraphic constraints on
851 canyon incision and Miocene uplift of the Central Andes in Peru. *Earth Planet Sci Lett*
852 263:151–166. <https://doi.org/10.1016/j.epsl.2007.07.023>
- 853 Valletta A, Carri A, Segalini A (2022) Definition and application of a multi-criteria algorithm to
854 identify landslide acceleration phases. *Georisk Assess Manag Risk Eng Syst Geohazards*
855 16:555–569
- 856 Wasowski J, Bovenga F (2022) Chapter 11 - Remote sensing of landslide motion with emphasis
857 on satellite multi-temporal interferometry applications: an overview. In: Davies T, Rosser
858 N, Shroder Risks, and Disasters (Second Edition) JFBT-LH (eds) *Hazards and Disasters*
859 Series. Elsevier, pp 365–438
- 860 Wasowski J, Bovenga F (2014) Investigating landslides and unstable slopes with satellite Multi
861 Temporal Interferometry: Current issues and future perspectives. *Eng Geol* 174:103–138
- 862 Yang W, Fang J, Liu-Zeng J (2021) Landslide-lake outburst floods accelerate downstream slope
863 slippage. *Earth Surf Dyn Discuss* 2021:1–19
- 864 Yang W, Wang Y, Sun S, et al (2019) Using Sentinel-2 time series to detect slope movement
865 before the Jinsha River landslide. *Landslides* 16:1313–1324
- 866 Zerathe S, Lacroix P, Jongmans D, et al (2016) Morphology, structure and kinematics of a
867 rainfall controlled slow-moving Andean landslide, Peru. *Earth Surf Process Landforms*
868 41:1477–1493. <https://doi.org/10.1002/esp.3913>
- 869 Zhou C, Yin K, Cao Y, et al (2018) Displacement prediction of step-like landslide by applying a
870 novel kernel extreme learning machine method. *Landslides* 15:2211–2225.
871 <https://doi.org/10.1007/s10346-018-1022-0>
872